Project no. **222422**

Project acronym: **ECCell**

Project title: Electronic Chemical Cell

Instrument: STREP/FET OPEN

Thematic Priority: Theme 3 Information and Communication Technologies

Deliverable n. 4.3: report, public (PU)

ECCell-based integration in microscale chemical processing networks.

Due date of deliverable: 31. 12. 2011

Actual submission date: 05. 03. 2012

Start date of project: **1.09.2008** Duration: **40 months**

Organisation name of lead contractor for this deliverable:

Ruhr-Universität Bochum (RUB-BioMIP), John McCaskill

University of Southern Denmark (SDU), Steen Rasmussen (section 5.13)

1. Deliverable 4.3: ECCell-based integration in microscale chemical processing networks.

1.1 Introduction

..

1.2 Final overall experimental platform in ECCell

To operate the chemical microprocessor platform, ancillary optical and electronic control and observation equipment is employed in addition to an external computer. Ultimately, all sensors, pumps and electronic control can be integrated onto the chemical microprocessor chip. Two or more syringe pumps are required to feed the basic module with chemicals and retrieve output or waste. Up to four additively combinable laser light sources at the standard wavelengths 488, 561 and 640 nm (DPSS 488 nm/100 mW (Coherent Sapphire 488-100 CDRH); Diode laser 640 nm/100 mW (Coherent Cube); DPSS 561 nm/100 mW (Oxxius OXX-561-100-COL-OEM)) illuminate fluorescently labelled chemicals to sense local concentrations via an EMCCD camera (iXon DV885, Andor), producing low-noise video rate images (1002 x 1004 pixels) that are readout and processed with custom software. A custom confocal optical setup using line-scan optics provides the required combination of high sensitivity and frame processing rate (to be published elsewhere). Averaged intensities of programmable subareas of these images are directly fed into the regulating algorithms to allow an online feedback based control of the chemical reactions taking place inside the module. A block-diagram summarizing the equipment is shown in fig. 18.

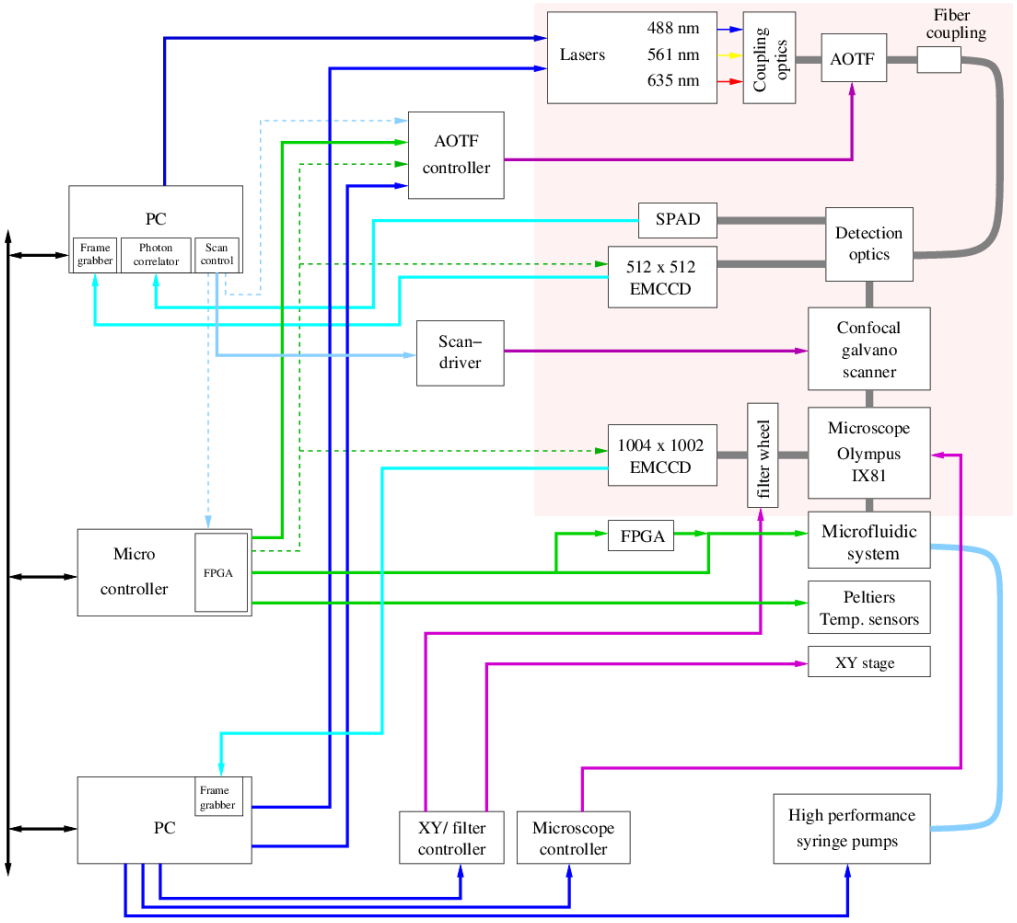

Figure 1: **Block-diagram of the experimental workstation control environment for the chemical microprocessor.** The lines between the blocks symbolize two-way control channels. Several computers, all connected via Ethernet, work

in a concerted fashion to coordinate the device controllers. The custom confocal optics support line and point scanning and photon correlation in addition to conventional fluorescence imaging. The custom interface computer (BioFox) provides flexible FPGA-based interfacing and synchronization between the PCs and the chemical microprocessor digital logic and other controlling devices..

System integration of the hardware is performed with a custom developed Linux based object-oriented control software written in C and GTK (GTK: Graphical Toolkit of GIMP, a public domain image processing library). The code contains around 200,000 lines of code, which integrates design files from our CAD entry tools (CAD tools: formerly Mentor Graphics Boardstation (TM), and currently Kicad, Jean-Pierre Charras, France) with all the communication protocols and APIs (application programming interface) of the various hardware devices, plus the images delivered by diverse cameras in the system (e.g. linking to the Andor EMCCD library). A major focus of the development was to create an easy-to-use GUI (graphical user interface) with comprehensive automatic documentation facilities. Especially the intimate coupling of camera images with feedback-control requires a tight coupling of the module designs with what is really seen in the microscope. In addition to pure experimental control software, a further camera device representing a real-time simulation package was written (see the section below on separation with coupled feedback controllers). This additional software-camera, seeing simulated molecular processing, not only allows us to test and validate new controller designs before implementing them in real hardware but also to serve as a world-model to extract parameters in chemical reactions that are not easily visible in the microscope.

1.3 New multilayer electronic design, fabrication & tests

In the course of the project there were numerous iterations to get reliable multilayer structuring of gold electrodes on our chemical microprocessor chips. During the development of the chip, BioMIP and the new cooperation partner on microfabrication iX-factory in Dortmund was faced with a variety of problems, which have been successfully solved in the last year of the ECCell project. Examples are e.g. the very high scrap rate following the reflow soldering process and several adhesion problems of the Gold metallization on wafer substrates as well. A series of fabrication strategies were explored to attain reliable multilayer structuring of gold electrode interconnect on our chemical microprocessor chips, with the final approach, developed by RUB together with iX-factory in Dortmund, resulting in a robust cross-over wiring of the chemical microprocessor chips.

The scheme in Fig. 19 shows the modified process flow designed by RUBa in collaboration with the iX-factory. Beside smaller technological changes, we integrated an additional platinum metallization step into our fabrication process to avoid the diffusion of Titanium atoms trough the gold film layer to avoid the formation of TiO_2 at the top of the gold layer. The latter would be very bad for the soldering process afterwards.

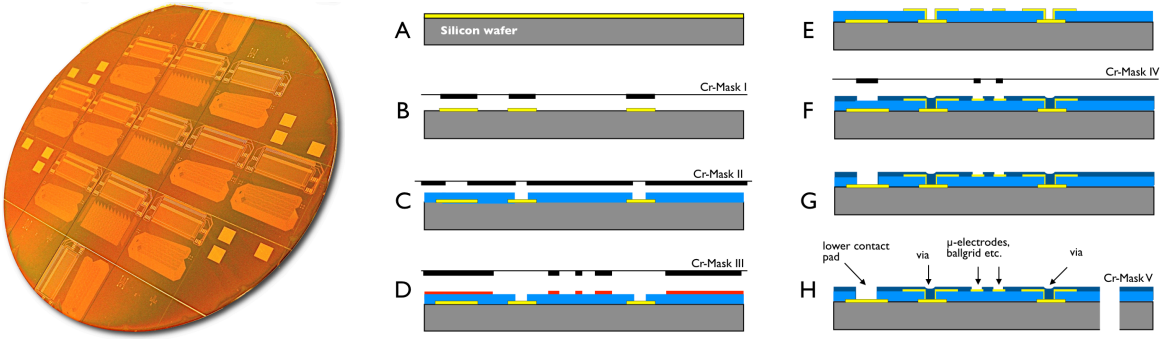

Figure 2: The left picture shows the new processed 6”-wafer. The right scheme shows the modified process flow for an user specific electrode multilayer design. Thicknesses of modified metal films: A: Ti (20 nm)/Pt (20 nm)/Au (200 nm)/ Ti (20 nm); D: Ti (20 nm)/Pt (20 nm) Au (200 nm).

The new modified fabrication process (Figure 19) starts with a lithographic step to structure the first conducting layer (Ti/Pt/Au/Ti) containing electrodes, wires and the vias for the upper (2nd) electrode layer (A and B). The following steps (C-E) are a passivation layer (SiO_2) deposition and a second Ti/Pt/Au metallization process and an etching procedure to realize the upper electrodes and wires and to complete via connections. After opening the 2nd passivation layer at the electrode and conducting pad areas, I/O holes were made using deep etching of the silicon substrate by Inductively Coupled Plasma (ICP) to allow a reverse side fluidic connection (F-H).

In the course of this process, we redesigned the single layer system for higher density electrodes and reimplemented the two-layer system within the new mask layout.

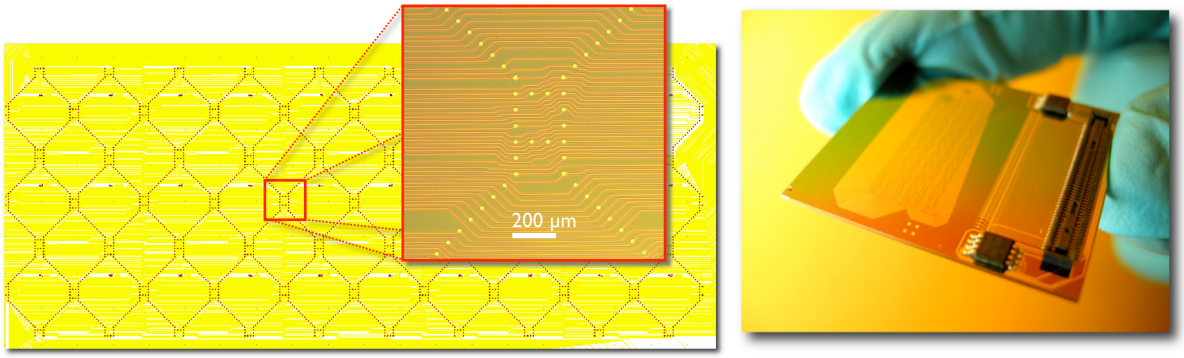

Figure 3: Left: Mask design based on basic FPGA 80 Inputs: 5338 microelectrodes controlled by 80 I/O-ports/chip (2.3 cm^2) Middle: The microscopic images showing the successful processed electronic layer of the double layer multilayer electrode array network. The right image shows the full-assembled electronic layer of the chemical microprocessor.

The new single layer layout contains a railway-like branching network of equally spaced electrodes, arranged in 48 blocks containing 82 individual controlled electrodes for cyclic molecular processing and transfer of molecular packets between different processing cycles.

Changing to a two-layer electronic chip design (figure 21), the integration density could be increased to more than 5.000 electrodes for the same chip space, which allows a high application potential for creating intelligent microfluidics in the ECCell project, e.g for travelling wave electrophoresis (TWE) on-chip. This two-layer design, developed in year one, was also adjusted for compatibility to the new metallization process and redesigned module interconnect.

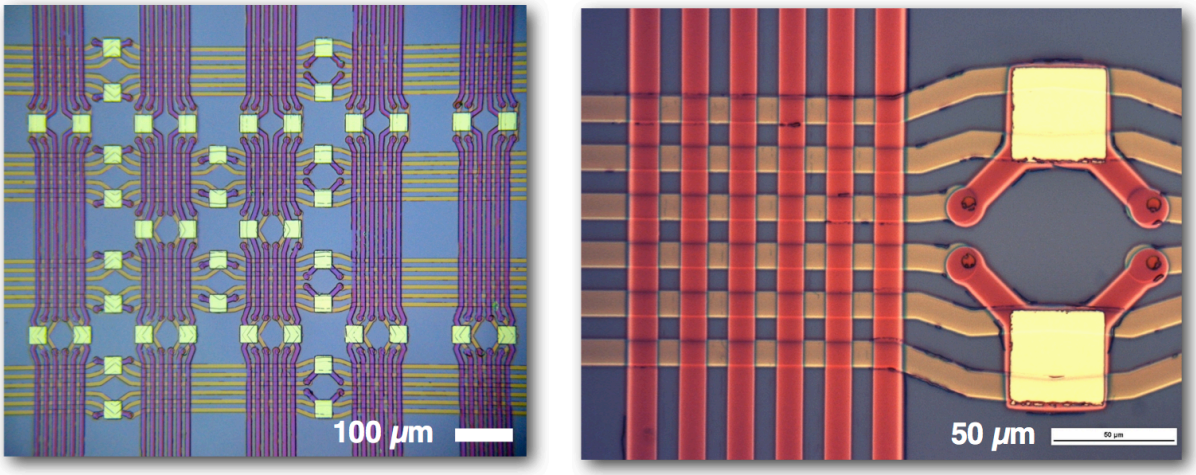

Figure 4: The light microscopic images showing the successful processed double layer multilayer electrode array network. The close-up (right) shows the exposed gold electrodes (gold) and two insulated (beneath SiO_2) layers of gold interconnect (red and brown shades in right picture).

The technological transition to the two-layer electronic chip design leads to an increased

integration density to more than 5.000 electrodes for the same chip space, which allows a more effective platform for future ECCells and other applications. Because connections are possible underneath the electrodes, the electrodes can also be made twice as large as in the single layer designs, which allows larger surface and diffusion-limited currents to be sustained. The production of these robust chemical microprocessors will be a lasting dividend of the project that can be exploited in a wide range of follow-on activities.

Development of a new adapter PCB

We developed a new adapter PCB (figure 22), which allows the direct connection to the BioFox board computer or to an electrochemical control system (e.g. cyclic voltammetry device). The jumpers rows allow flexible choice of input and the FPGA programmable control sequences for the electrodes.

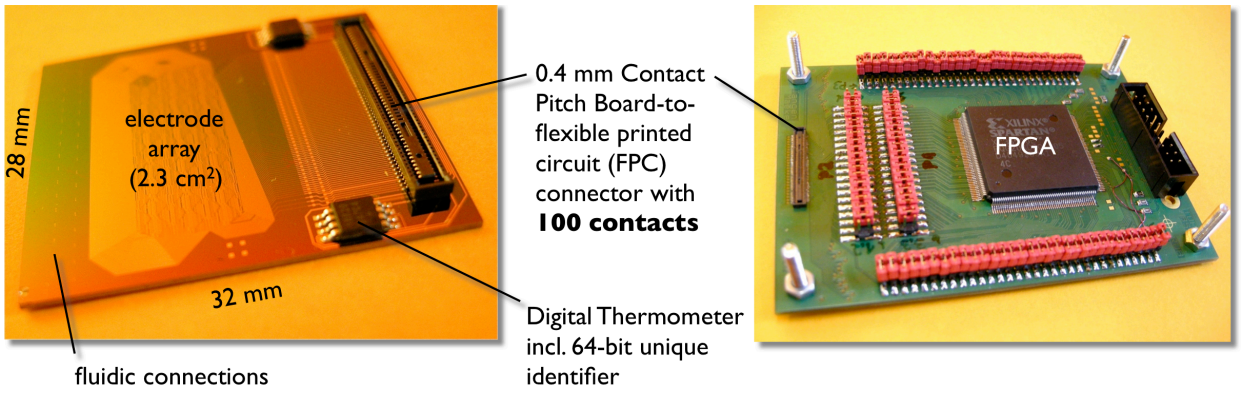

Figure 5: Left: The full assembled chemical microprocessor chip. Right: The new adapter PCB allows the direct connection to the BioFox board computer or to an electrochemical control system.

In summary, the main advantages of the new microsystem we built up are as follows:

- it is easier to establish low-noise and variable voltage electrochemical interfaces to the chip
- the fabrication and assembly of the chip is significantly easier and more cost-efficient
- the FPGA has been moved to the adapter PCB, this enables a more efficient & reliable packaging of integrated circuits
- integrated temperature control & an unique identifier (this makes a depository of such chips manageable)

In addition to the work on these chips, extensive software work was performed to program the reconfigurable chips to support programmable electronic switching with variable voltage levels (see also WP5 and D5.3).

Electrogenerated Chemiluminescence (ECL) for direct optical control of 2layer µ-electrodes

We used a new procedure based on ECL, which allows direct optical control of the complex μ-electrode array to check the fabrication quality of the electrodes as well as the programmed sequences. ECL using Rutheniumbipyridyl catalysts were shown 1981 by Rubinstein[1]. In 1990 Leland and Powell[2] did some pioneering work using the Ru-catalyst together with

[1] Rubinstein, I. *Electrogenerated Chemiluminescence* JACS, 103, 512–516.

[2] Leland J K and Powell M J *Electrogenerated Chemiluminescence: An Oxidative-Reduction Type ECL Reaction Sequence Using Tripropyl Amine* J. Electrochem. Soc. 137, 3127.

Tripropylamine (TPA), and this has been improved by the Manz group and partly integrated in microsystems[3].

The redox system based on a buffered electrolyte solution (0.1 M phosphate buffer, pH 6.9) containing 5 mM $Ru(bpy)_3^{2+}$ and 25 mM TPA. Small Voltage triggers the ECL reaction. Ruthenium and TPA are excited in the process. The TPA radical serves as a reductant enabling Ruthenium to turn to his base state with the release of light. The cycle of electrochemoluminescence repeats as long as voltage is applied, resulting in an amplification of the light signal. The EMCCD camera can detect the emitted fluorescence signal (λ_{max} = 610 nm).

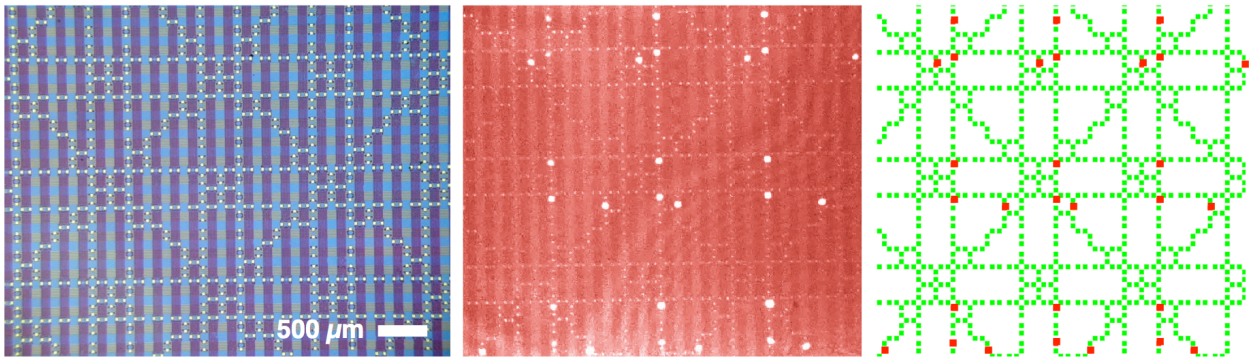

Figure 6: **Experimental actuation and sensing network realized in the project in a thinned ("fractal") electrode space.** The direct optical monitoring of the double layer multilayer electrode array network using electrochemiluminescence ECL is shown in the middle panel. Left: Light microscopic image of a small portion of the microelectrode array, connected by two-layer wiring. Middle: Fluorescence image of an electrochemically active test chemical layer covering the electrode array (0.1 M phosphate buffer electrolyte solution (pH 6.9) 5 mM $Ru(bpy)_3^{2+}$, 25 mM TPA and 100 µM benzyl viologen. (ΔE_{elec}=1.8V, λ_{max} = 610 nm)). Right: Snapshot of an electronically programmed sequence of electrode activation, showing activated electrodes in red. Note the perfect transfer of this activation pattern to chemical changes in the solution, and their optical detection, closing the feedback loop as input to the electronic layer for further computed changes in electrode activation.

We successfully tested the system in ultra-thin fluid films on-chip (figure 23). Only one droplet of the potential redox solution was placed onto the multi-electrode array and covered with a thin glass slide (thickness 120 μm). To find out the optimal configuration we triggered a couple of microelectrodes with different digital voltages 1.8, 1.7 and 2.5 V (figure 24).

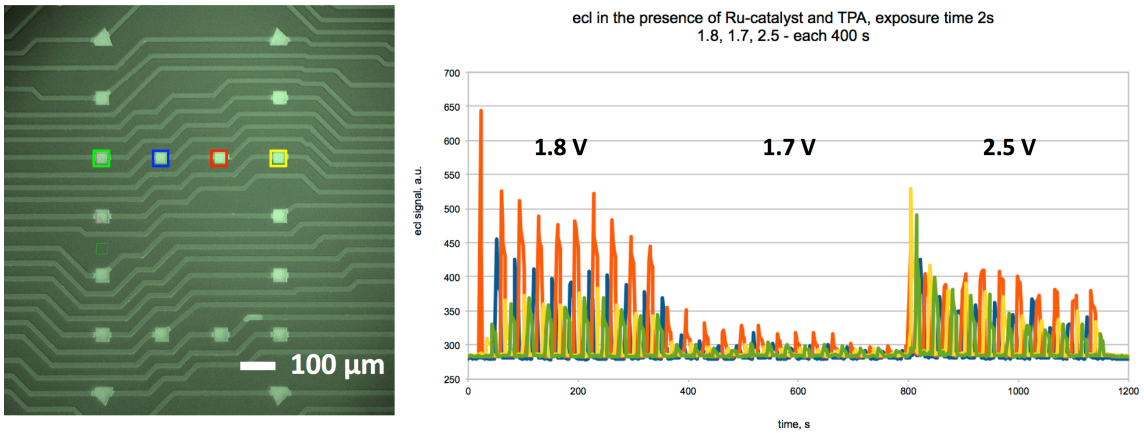

Figure 7: **On-Chip ECL optimization.** Left: Light microscopic image of µ-electrodes. Right: Fluorescence intensity measurements within the squared coloured sensor elements above the electrodes. Redox solution: 0.1 M phosphate buffer electrolyte solution (pH 6.9) 5 mM $Ru(bpy)_3^{2+}$, 25 mM TPA and 100 µM benzyl viologen. (ΔE_{elec}=1.7, 1.8 and 2.5 V, λ_{max} = 610 nm).

[3] Arora A, Eijkel J C T, Morf W E and Manz A *A Wireless Electrochemiluminescence Detector Applied to Direct and Indirect Detection for Electrophoresis on a Microfabricated Glass Device* Anal Chem 73 3282–3288.

This method allows us to get very good direct optical control of μ-electrodes with fast response, which is useful for perform quality control, helpful to observe conducting problems as well as to find software problems with regard to program the electrode sequences. It works for low digital voltages in the range between 1.1 and 2.5 V.

1.4 Programmable injection, extraction, mix and split operations

To complete the experimental test of our electronically domain structured generic chemical microprocessor, we evaluated the ability to process DNA from two flowing, dilute aqueous solution domains (which could be used as inputs and outputs) in an intervening gelled domain under electronic control. The transfer of informational molecules from the liquid to the gel phase is a prerequisite for renewable processing in a continuous flow setup.

The image series in figure 11 (rotated 90° wrt fig. 1) shows an excerpt of a test fluidic structure for this, consisting of three (horizontal) microfluidic channel domains, which are interconnected through (vertical) domain barrier channels (channel height ca. 1 μm as above). The middle channel was filled with the hydrogel and the upper and lower domain channels contained DNA oligonucleotides flowing in his-buffer at a very slow velocity (1 μl/h).

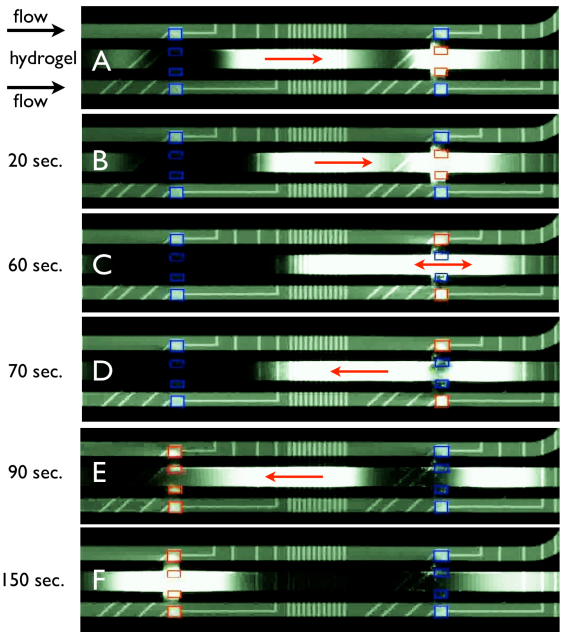

Figure 8: **Move, mix and split operations.** The middle channel filled with: 25% Pluronic F87/F127 (2:1) copolymers T_m = 37°C side channels: $1x10^{-6}$M 3'-Alexa488-GTT CAT CG-5' (8-mer) in 50mM histidine-buffer.

After concentrating the fluorescence labelled oligonucleotides in the gel phase, we demonstrated the basic functions of the system: selective transport (A, B, E, F), mixing (C) and splitting (D) operations. Almost complete decoupling of the processing in the central gel domain from the connected aqueous flow domains was achieved, through a suitable choice of electrode potentials, *i.e.* without field gradients along the shallow domain bridges.

1.5 Travelling wave functionality with non-blocking electrodes in µ-channels

One of the objectives in using travelling wave functionality in the chemical microprocessor is a modulation between separative and non-separative transport in channels. The following two experimental examples demonstrate the manually electrode control for non-separating and separation transport applications.

Programmable non-separative molecule transport in microfluidic channels

This experiment shows the non-separative transport using a manually programmed sequence

(Figure 26) by the ng_biopro software package.

Sequences (B)-(D) show the concentration and transport of the oligonucleotides in one direction and the movie sequences (E)-(G) in the other direction of the microfluidic gel-separation channel. The image (I) shows the process of the reversible melting of the Pluronic-Gel-Mixture at 10°C and the inflow of new probe solution. After that the system is back in his initial state (H).

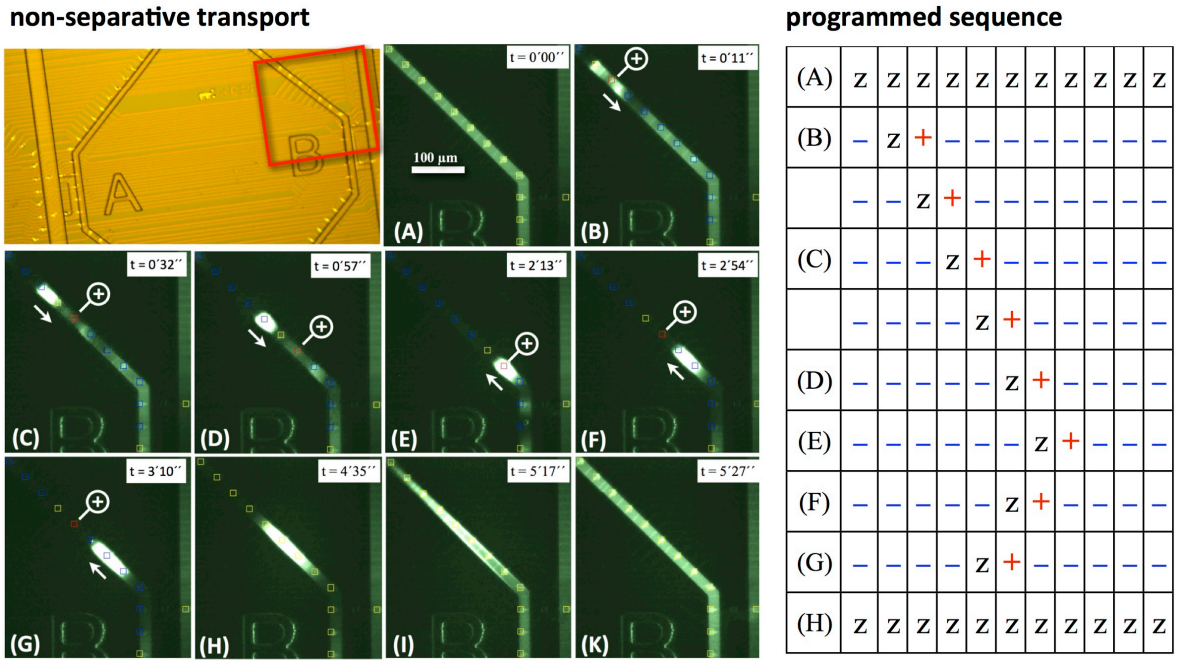

Figure 9: **Non-separative transport using a manually programmed sequence:** 30% Pluronic 127/87 hydrogel 1:2, DNA mixture: 3`-CA AGT AGC-5` Alexa488 and Alexa647 labelled 5`-TTT TTT TTT TTT TTT TTT TT -3` Hexyl ($2x10^{-7}$M) in 50 mM Histidine-buffer. pH 7.2

Programmable separative transport (without feed back control)

We tested the formation of renewable sol-gel boundaries at defined locations using the F87/F127 Pluronic® hydrogel mixture also for separative transport in our chemical microprocessor. The gelation of the hydrogel mixture is reversed by cooling down to 10°C. Once the separation process is finished we could restart the flow and wash out the separated material. A second heating step led to renewed gelation and then the next separation cycle could be performed.

To start the separation process, the electrodes in the gelled domain channel (marked in red circle) were turned on both DNA strands. They began to migrate to the positively charged electrodes. The oligomers were separated by the different mobilities (figure 27, left image).

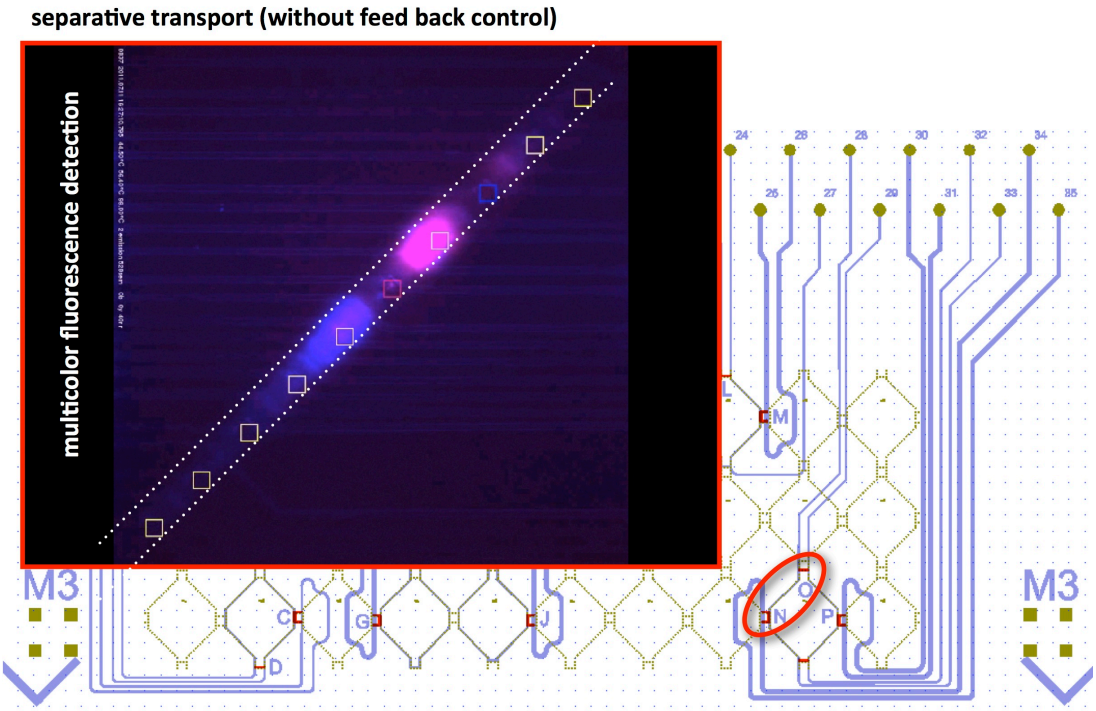

Figure 10: **Separation of two different length DNA oligonucleotides (lengths 24 and 30 nts)**: Channels 28 and 29 are filled with 25% Pluronic (F87 : F127) 1:1 in His 50mM pH 7.2; OligoN (24-mer) Alexa647 10^{-7} M + Oligo4 (30-mer) Dy481XL 10^{-6} M Channels 30, 31, 34, 35 are filled with H_2O; T = 19.7°C.

1.6 Feed back controlled Traveling-Wave Electrophoresis in microfluidic channels

To establish feedback controlled travelling-wave-electrophoresis a sequential set of state-machines was designed and executed, see the following Scheme 4.1. After initialization (command 'control_add') a distributed sequence of state-machines is executed. The algorithm is such that the originally even distributed DNA in the Pluronic-gel-matrix is collected and then separated. Up to the execution of the separation state-machine 'separ1' the material is transported back and forth in the channel. When the cluster of DNA is reaching the beginning of the channel separation is enacted. Two electrodes with opposite polarity and far away (one at the beginning of the channel and the second at the end) are activated. Due to different mobility both oligo-types (Oligo1 and Oligo20, see Figure 28) separate enough to automatically switch an electrode with a negative potential in between the two separating clusters. This is the effective separation event. The timing is derived from sensors (rectangular areas in the camera-image) which indicate when the forefront of the separating cluster arrived at a certain location. Two electrodes before, a single electrode is then used as the cloud-cutter. The slower cluster, in this case Oligo1, is actively transported back in the channel whereby the faster cluster is left untouched.

```
#-------------------------------------------
# ng_biopro_i686 -batch ng_biopro_auto_shift_8.cmd -cam 0x80 -design 61 -fluid M3
#-------------------------------------------
echo eval_channel design/fluidic/biopro61_std/M1_B5_SEG.dat
eval_channel design/fluidic/biopro61_std/M1_B5_SEG.dat

echo control_add autoshift1 "general" r1833
control_add autoshift1 "general" r1833
control_add autoshift2 "general" r1834
control_add autoshift3 "general" r1835
control_add autoshift4 "general" r1838
control_add autoshift5 "general" r1839
control_add autoshift6 "general" r1844
control_add autoshift7 "general" r1843
control_add autoshift8 "general" r1842
control_add autoshift9 "general" r1841
control_add autoshift10 "general" r1840
control_add autoshift11 "general" r1833
control_add separ1 "general" r1833
control_add autoshift12 "general" r1843
control_add autoshift13 "general" r1842
control_add autoshift14 "general" r1841
control_add autoshift15 "general" r1840

auto_shift_8 autoshift1 r1833 r1834 r1835 r1838 r1839 r1840 autoshift2
auto_shift_8 autoshift2 r1834 r1835 r1838 r1839 r1840 r1841 autoshift3
auto_shift_8 autoshift3 r1835 r1838 r1839 r1840 r1841 r1842 autoshift4
auto_shift_8 autoshift4 r1838 r1839 r1840 r1841 r1842 r1843 autoshift5
auto_shift_8 autoshift5 r1839 r1840 r1841 r1842 r1843 r1844 autoshift6
auto_shift_8 autoshift6 r1844 r1843 r1842 r1841 r1840 r1839 autoshift7
auto_shift_8 autoshift7 r1843 r1842 r1841 r1840 r1839 r1838 autoshift8
auto_shift_8 autoshift8 r1842 r1841 r1840 r1839 r1838 r1835 autoshift9
auto_shift_8 autoshift9 r1841 r1840 r1839 r1838 r1835 r1834 autoshift10
auto_shift_8 autoshift10 r1840 r1839 r1838 r1835 r1834 r1833 autoshift11
auto_shift_8 autoshift11 r1833 r1834 r1835 r1838 r1839 r1840 separ1
separ1 separ1 r1833 r1844 r1847 autoshift12
auto_shift_8 autoshift12 r1843 r1842 r1841 r1840 r1839 r1838 autoshift13
auto_shift_8 autoshift13 r1842 r1841 r1840 r1839 r1838 r1835 autoshift14
auto_shift_8 autoshift14 r1841 r1840 r1839 r1838 r1835 r1834 autoshift15
auto_shift_8 autoshift15 r1840 r1839 r1838 r1835 r1834 r1833 autoshift1
```

Scheme 4.1: Shown is the low-level control language of the ng_biopro-software which defines the feedback-controlled TWE, see also Figure 4.7 and the movie ng_biopro_vid_20111019_1505xxx_0_elec.mpg in the supplementary material.

In the first part of scheme 4.1, with the command control_add, several feedback-controllers are initialized and distributed along a channel. The second part contains the state-machines, which establish the chain of feedback-controllers along the channel. Execution starts at controller ‘autoshift1’ (state-machine is ‘auto_shift_8’ which is specified in Scheme 4.1). The first part is moving a cluster of DNA until a separation event can happen which is realized via a second state-machine ‘separ1’. After separation the left cluster is moved back in the channel and the right cluster is left at its current place.

The state-machine used to transport the clusters of is shown as a diagram in Scheme 4.2 (Left) and in the control-language notation in Scheme 4.2 (Right text box).

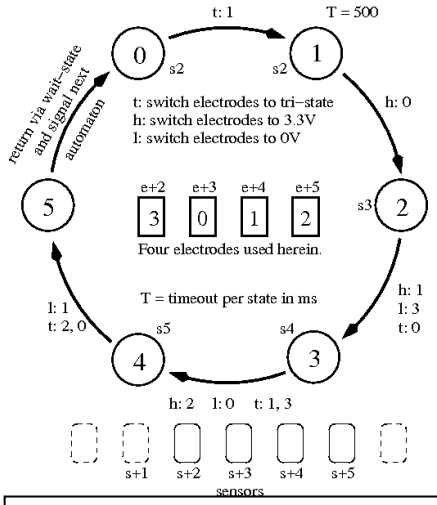


```
control_group $1 0 $3
control_group $1 1 $4
control_group $1 2 $5
control_group $1 3 $2
control_sensor $1 $3 $4 $5
control_reference $1 $2 $3 $4 $5
set_sensor sen_$2 high_thr 1.70
set_sensor sen_$3 high_thr 1.70
set_sensor sen_$4 high_thr 1.70
set_sensor sen_$5 high_thr 1.70
nr_states $1 6 # 0->1 event=1, 1->0 event=0
# name state sensor event prio. tiout nstate
nrhigh {list} nrlow {list} nr-tri {list}
add_state $1 0 sen_$2 1 5 0 1 0 0 1 1
add_state $1 1 sen_$2 1 5 500 2 1 0 0 0
add_state $1 2 sen_$3 1 5 0 3 1 1 1 3 1 0
add_state $1 3 sen_$4 1 5 0 4 1 2 1 0 2 1 3
add_state $1 4 sen_$5 1 5 0 5 0 1 1 2 2 0
add_state $1 5 $6 1 5 0 9999 0 0 0
```

Scheme 4.2: Left: State-machine diagram to transport DNA oligos. Sensors are coincident with electrodes with the only different the eight times larger area when compared in the camera image. This state-machine has six states and at the end is signalling the following state machine to commence operation. Separation is then realized via a second state-machine which declaration can be seen in Scheme 4.3. The resulting video can be seen in the supplementary material as ng_biopro_vid_20111019_1505xxx_0_elec.mpg. See also Figure 4.7 as an overview of the whole experiments with all chemical details used within. Right: The six-state state-machine used to transport the molecules along the chain.

```
#-------------------------------------------
# ng_biopro_i686 -batch ng_biopro_auto_shift_8.cmd -cam 0x80 -design 61 -fluid M3
#-------------------------------------------

control_group $1 0 $2
control_group $1 1 $4
control_sensor $1 $2 $3
control_reference $1 $2
set_sensor $1 sen_$2 high_thr 8.8
set_sensor $1 sen_$3 high_thr 5.5   # Threshold for separation
nr_states $1 3
#                0->1 event=1, 1->0 event=0
#          name state sensor    event pri. tout nstate nrh {list} nrl {list} nrt
{list}
add_state $1   0   sen_$2      1    5    0     1     1    1     1    0     0
add_state $1   1   sen_$3      1    5    0     2     0          0          2    0 1
add_state $1   2    $5         1    5    0  9997     0          0          0
```

Scheme 4.3: **The state-machine declaration for separating the DNA molecules.** Only after the separating cluster has

reached a certain distance (sensor sen_$3 with threshold 5.5) from the beginning an electrode which is then presumably located in between the two separating clusters is switched to a negative potential. This effect is realized via giving control to the next state-machine (depicted by parameter $5) which then takes the slower cluster to be transported back.

Though separation worked in this experiment we have to admit that a reproducible separation remains a challenge. Especially the frequent observation that the two clusters due not separate significantly and stay attached at each other. What the specific reason for this strange behaviour is, is not yet known and we are working hard to find a solution to this problem.

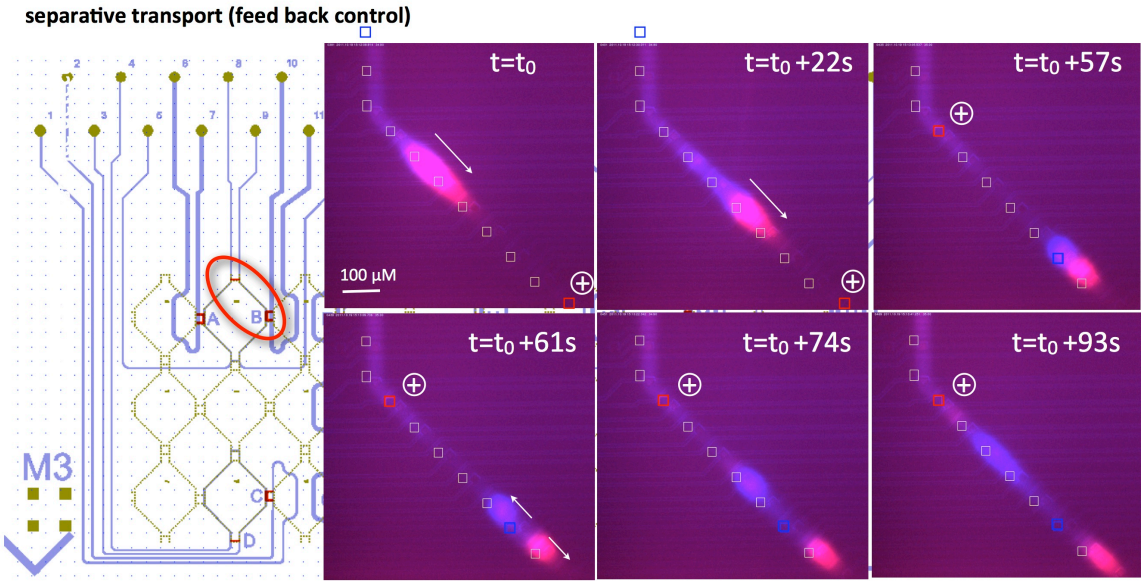

Figure 11: **Selective transfer of DNA between sites under autonomous feedback electronic control.** Two different oligonucleotides (labelled red and blue) in a mixture could be autonomously separated and one transferred to a second reaction site by the coupled two-layer electronic-chemical sensor-actuator system developed in ECCell. Channel 9 is filled with 30% Pluronic (F87 : F127; 2:1) in His-buffer 50 mM pH 7.2 + 5 mM Na_2HPO_4 Oligo20 (8nt) Alexa647 10^{-7} M + Oligo1 (30nt) OregonGreen 10^{-7} M. Channels 10, 11, 5 and 8 are filled with H_2O. Pluronic melting temperature T_m = 22°C.

1.7 New microfluidic experimental designs - twin chamber molecular amplification module

During the third project year, new microfluidic experimental designs were realized to achieve the microfluidic integration of DNA-templated amplification reactions (Montagne system, pH depended triplex replication) in a twin chamber reactor. Figure 29 shows two alternative versions of microfluidic systems for electronically regulated amplification in ECCell we used for experiments regarding content processing into separation gel and TWE optimization tests.

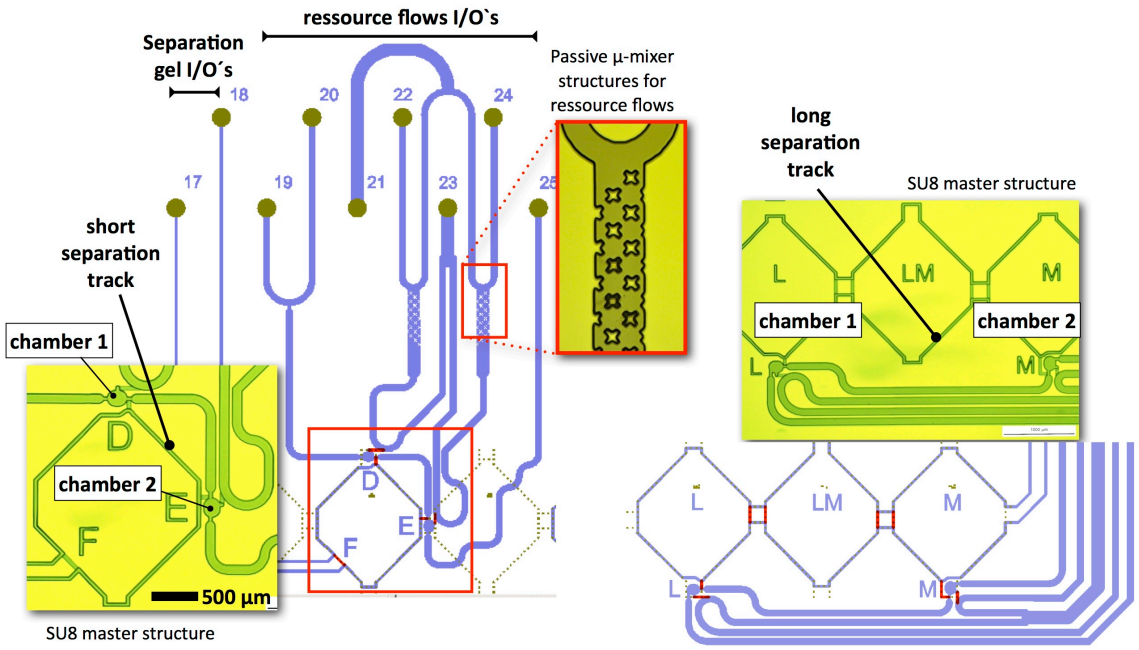

Figure 12: **Two microfluidic twin chamber designs for electronically regulated isothermal amplification in ECCell.** The basic architecture involves three types of chemical channels: (i) continuously flowing resource channels supplying nutrients and removing waste (21-24) (ii) mostly static segmented (two-phase) chain of chemical reaction chambers that can be stepped through the system for diagnostic purposes (19,20,25) (iii) static gelled chemical separation and communication channels (17,18). In the full architecture, the communication network connects pairs of such chambers to other pairs (see section 6) for proliferation and cooperation. The complexities of the supply channel and geometry are dictated here in part by the desire to perform analytical chemical work to diagnose the performance of the ECCell operation: the segmented structure in (ii) allows the contents of individual local chemical reactions to be extracted from the device for analysis.

The left two chambers elementary module is a single ECCell for cyclic processing of DNA with iterative product separation & feedback functionality for first tests regarding the programming of the fluid transfer element, which connect the fluid and gel channels.

1.8 Twin chamber replication scheme for selective transport of DNA species

Twin-chamber DNA replication based on conformational switch relies on immobilization and strand displacement mechanisms. The immobilization of short building blocks is limited by stability of duplex under certain conditions. Therefore, at this stage we could manage only DNA amplification involving full length pieces (Figure 30).

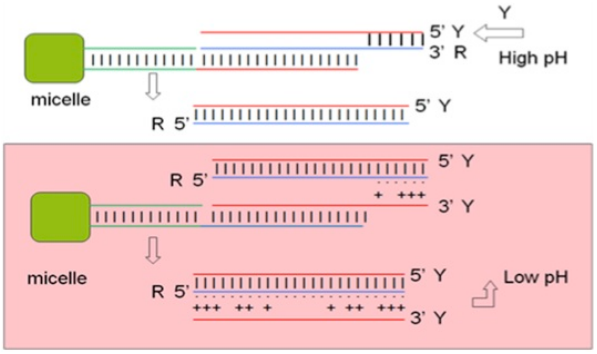

Figure 13: Toe-hold strand displacement mechanism.

The dyes are attached to 5'-ends of the fuel strands, so they can in principal change hybridization, most probably creating no problems for our amplification. Further sequence-specific release of templates involving toe-hold strand displacement would allow selective transport of duplex and triplex fractions at high and low pH, respectively.

Sequence design for toe-hold strand release mechanisms:

- **“A”:** 5' UUU UGC GGA TTC, 12-mer micelle-forming strand

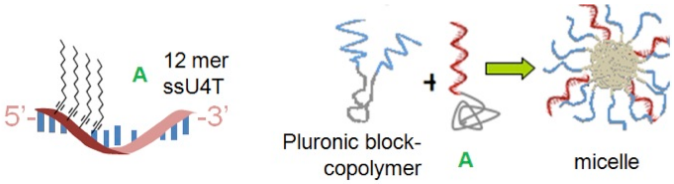

- **“B”**: 5' GAG AAA AAA GAG GAA GGG GAA TCC GCA AAA, 30-mer which forms 18 base pairs with "Y" leaving 6 nt of "Y" free for toe-hold at 3' end for strand displacement.
- **“C”:** 5' CTC TTT TTT CTC CTT CCC GAA TCC GCA AAA, 30-mer which forms 18 base pairs with "R" leaving 6 nt of "R" free for toe-hold at 3' end for strand displacement.

We were pursuing the aim to orchestrate triplex amplification in twin-chamber involving selective transport of product monitoring its growth (Figure 31).

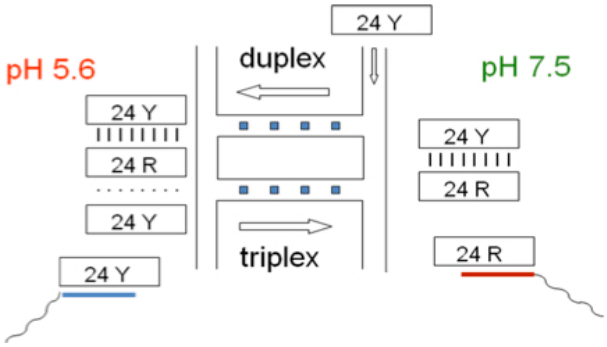

Figure 14: **Twin-chamber replication scheme.** Templates initially are immobilized.

Twin-chamber replication would involve constant pH for the hybridization of full length strands Y and R within duplex or triplex. The hybridization would allow toe-hold strand displacement only of a "fuel" portion. To achieve that and therefore prevent product transfer of templates we put efforts into sequence-specific immobilization of templates (Figure 32).

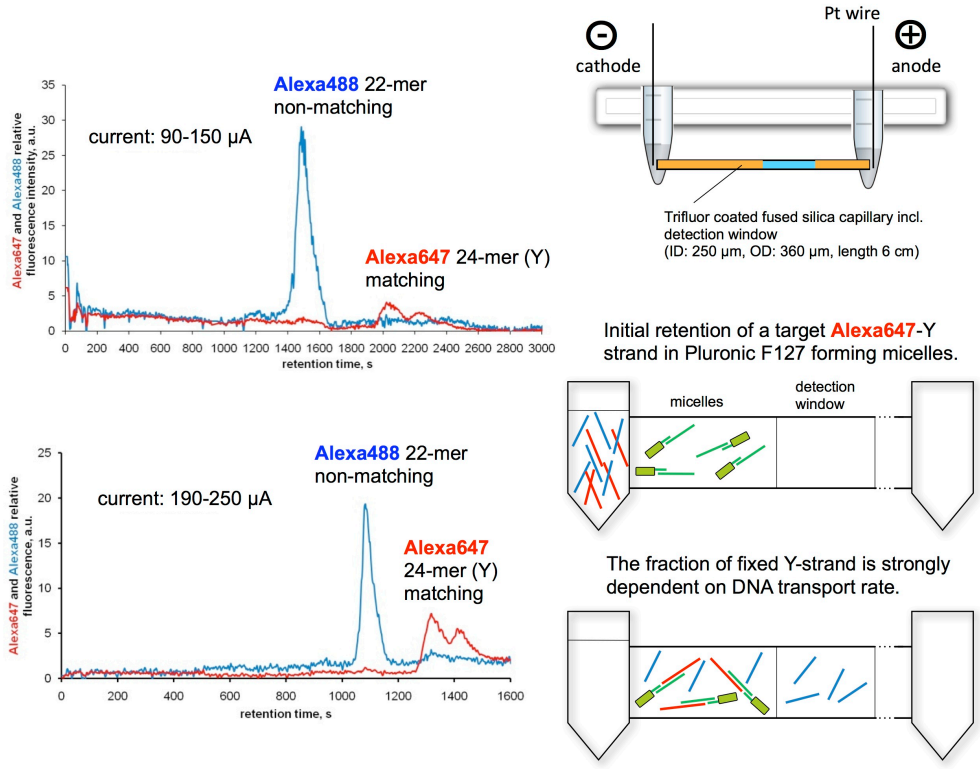

Figure 15: **CGE test of DNA retention in Pluronic.** The retention was concerned with formation of micelles involving four alkyl chains from 12-mer hybridized with a connector strand (green). Target strand is followed by Alexa647 fluorescence (red). The Alexa647 fluorescence concerned with a DNA fraction, which was retarded, is plotted red. The Alexa488 fluorescence of a not matching control is plotted blue. A capillary containing Pluronic with micelles was connected with a capillary containing only Pluronic via a silicon adapter (right side). Two CGE runs are shown with different currents achieved (left side).

We employed CGE for fast DNA fraction analysis following laser-induced fluorescence of dyes at two wavelengths. Low amount of "R" can hybridize 6 bases of fuel "Y" forming 24 bp duplex YR. At high pH formation of duplex involving toe-hold strand displacement occurs within 40 min (Figure 33, at the top). At low pH duplex YR can also hybridize second Y-strand forming triplex fraction followed by two colours detection (Figure 33, at the bottom). Transfer of duplex and triplex was detected in a separation channel connected to the micelle container via silicon-adapter.

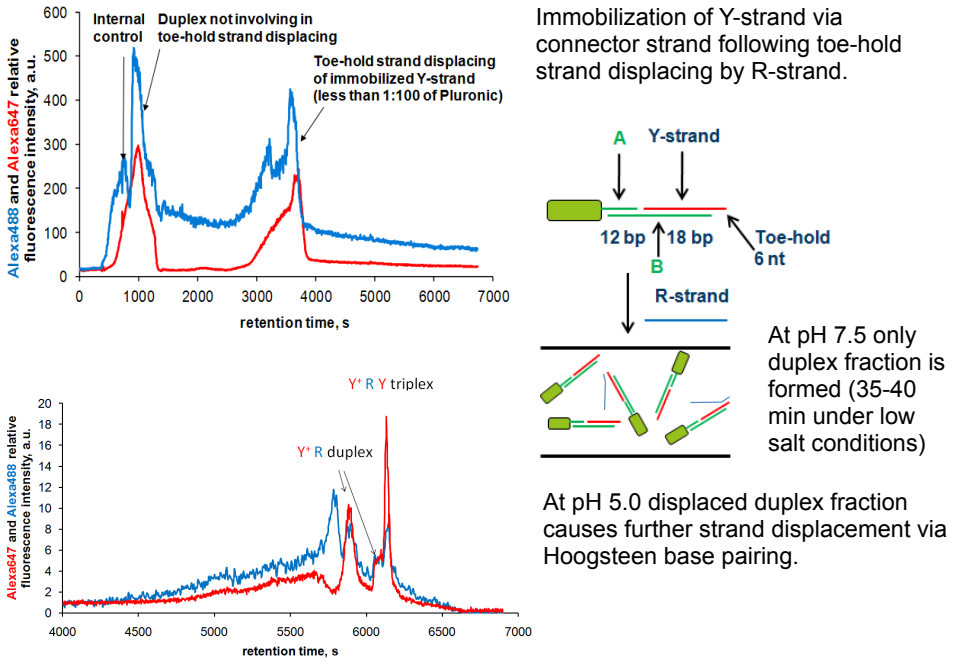

Figure 16: CGE test of DNA toe-hold strand displacement. The release was concerned with toe-hold strand displacement via 6 nt (red). Target strand is followed by Alexa647 fluorescence. The Alexa647 fluorescence concerned with a DNA fraction, which was initially retarded (Figure 2.6) and then released, is plotted red. The Alexa488 fluorescence of a not matching control is plotted blue. First diagram is obtained at pH 7.5, second - at pH 5.0 involving duplex and triplex formation, respectively.

Amplification of Alexa488 fluorescence is expected while moving stuff towards low pH chamber, amplification of Alexa647 while moving stuff towards high pH chamber. Triplex and duplex formation is supposed to take 40-60 min time, separation in CGE could take up to 40 min dependent on the current.

Triplex shows promising pH-dependence and also rate of formation. Micelle-forming strand would contribute to better retention if contained 18 bases instead of 12. Low salt condition limitations of triplex applications in microfluidics are overcome by large concentrations of the strands achieved inside Pluronic. In conclusion, everything required twin-chamber enzyme-free amplification is established.

1.9 Sequence specific DNA retention with ECCell gels in µ-channels

Figure 34 shows the electrokinetic repulsion as well as attraction of non-matching DNA **"X"** and matching DNA **"R"** in a matrix of immobilised ssU4T-12 in Pluronic gel using microelectrodes in a microfluidic channel (dimensions: 40 μm width, 30 μm depth).

Sequence design:

- **"A12":** 5' UUU UGC GGA TTC, 12-mer micelle-forming strand
- **"A18":** 5' UUU UGC GGA TTC GTC TGC, 18-mer micelle-forming strand

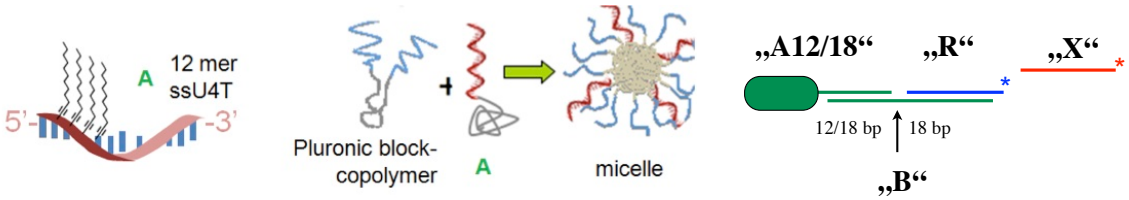

- **"B":** 5' CTC TTT TTT CTC CTT CCC GAA TCC GCA AAA, 30-mer which forms 18 base pairs with "R" leaving 6 nt of "R" free for toe-hold at 3' end for strand displacement.

- **“R”:** Alexa488-5' GGG AAG GAG AAA AAA GAG GAA GGG (matching strand)
- **“X”:** Alexa647-5'CGA TGA ACC TGC GTG A (non-matching strand)

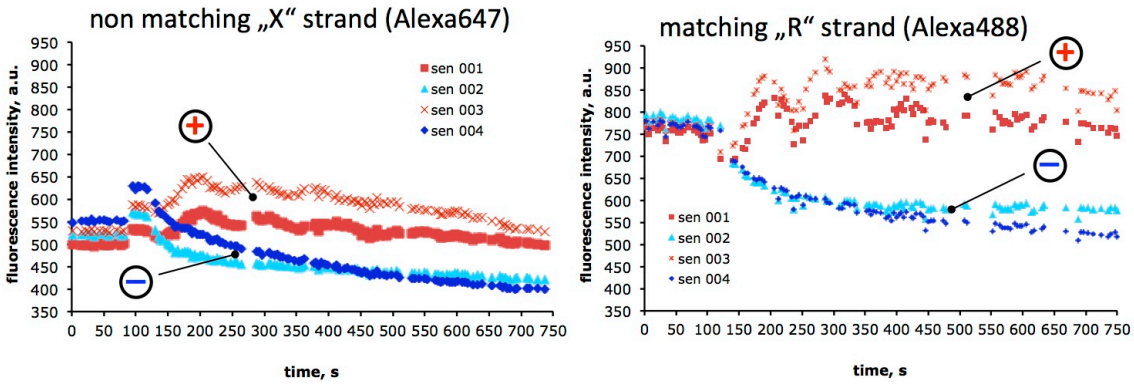

Figure 17: The plots show that negative charged electrodes repel the non-complementary as well as the complementary strands. Positive charged electrodes lead to a concentration of the non-matching as well as the matching species too. Non-matching DNA was labelled with Alexa647, matching DNA - with Alexa488. Experimental conditions: 29°C, immobilised ssU4T-12 (5 µM) in 18% w/v Pluronic F127. Excitation wavelength: 488 nm and 647 nm; U=1.8 V. (120130).

We observed that the slope corresponded to kinetics of DNA concentration (figure 34, right plot) at selected electrodes (Figure 35, left image), is higher for non-matching DNA. Furthermore, the concentration factor we calculated subtracting background and dividing the value at maximum to initial value of fluorescence is higher for the non-matching species (Figure 35, middle). Oscillations in fluorescence intensity obstruct the analysis of data taking into account duty cycle (U=1.8V, 40 %) and possible quenching due to high DNA concentration (5 μM).

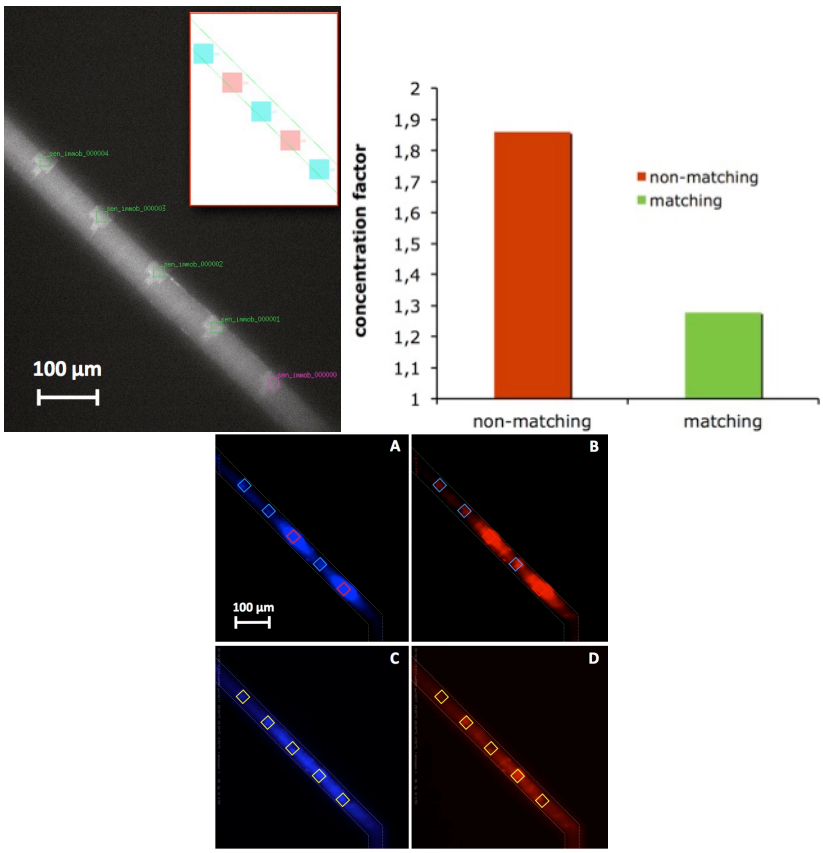

Figure 18 Left: Fluorescence image of the microfluidic channel and selected microelectrodes. Middle: Calculation of the concentration factor. Right: Concentration using positively charged microelectrodes (red colored squares) of matching **“R”** (A) and non-matching DNA **“X”** (B). Electrode are switched off in (C) and (D).

Figure 36 demonstrates the concentration of matching and non-matching DNA in a matrix of immobilised U4T-18 **A18** in Pluronic. The experiment shows no significant difference between U4T-12 **A12** and U4T-18 **A18**, both are working with slight selectivity towards matching DNA as calculated above.

The concentration factor was only 1.9 for non-matching DNA, taking into account that we used maximum values at the initial fluorescence enhancement although it was then decreasing and created oscillations in the fluorescence intensity. More importantly, we found slower kinetics of the concentration at the electrode observed for U4T-18 in respect to one observed for U4T-12.

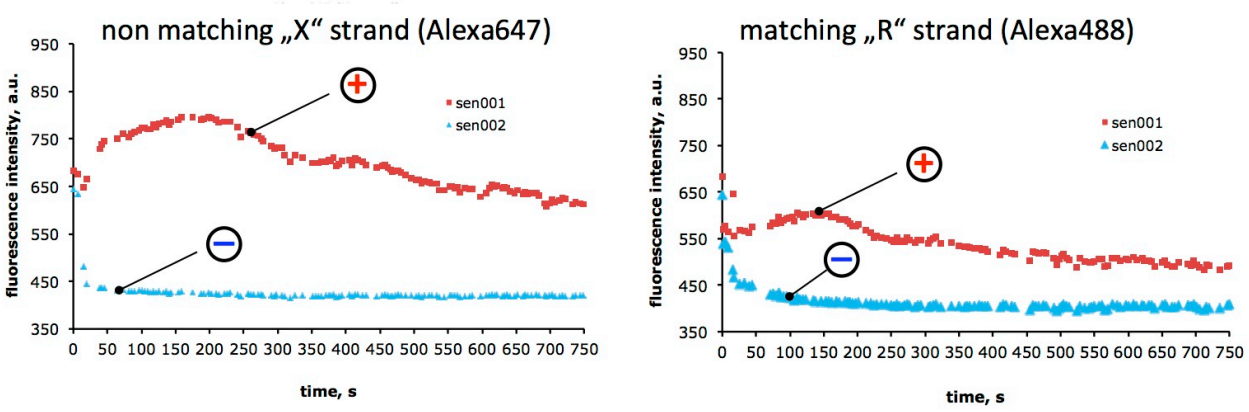

Figure 19: Concentration of matching and non-matching DNA in a matrix of immobilised U4T-18 **A18** in a Pluronic gel.

1.10 Exponential enzymatic amplification system in small reaction volumes

We established *in vitro* DNA oscillator of K. Montagne in microliter scale (see also cf. WP1) as an alternative route for the development of replication systems in microfluidics and show that is a much more powerful system than linear SDA.

Figure 37 shows a concept of a two chamber DNA enzymatic amplification procedure. In this system two 22-mer DNA strands produce primers for its own replication via polymerization in a concert with nicking and strand displacement. When immobilized at two separate chambers, DNA strands would produce primers. Primers would be transferred from one chamber to other following fluorescence of the marker molecule (11-mer). The immobilized strands would contain Alexa488 and Alexa647 dyes at 5'end suitable for the optical setup arranged, so if necessary, they would get through digestion by exonuclease *RecJf*.

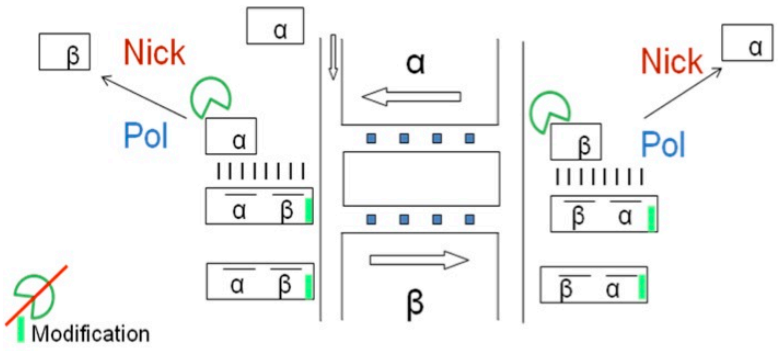

Figure 20: Twin-chamber microfluidics to arrange transfer of primers for nSDA to support overall exponential growth of output.

In WP1 RUBb synthesized templates with 3'phosphate and two 5'phosphorothioate substituted nucleotides: T1, T2, and T3. Accordingly Montagne et al. modifications prevent

digestion of DNA in the presence of exonuclease RecJf. Exonuclease was introduced as a principal participant in the oscillator to remove inhibitor and let α concentration to grow up again. Accordingly, in the presence of exonuclease RecJf, the inhibitor was digested as efficiently as long RecJ was incubated with complex template-inhibitor (Figure 38, left).

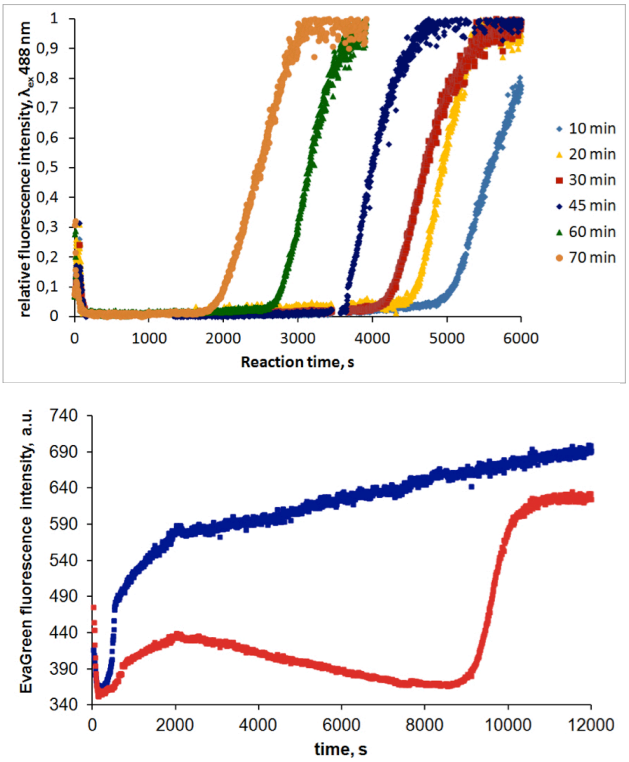

Figure 21: Left plot: Growth of ααT1 (100 nM) in the presence of RecJ (30 u/ml). Although inhibitor (100 nM) wasn't pre-hybridized with template at high temperature it was affected by exonuclease resulting in time-shift of the curves accordingly to the treatment time. Right plot: Observation of amplification, inhibition and digestion actions working in a concert. Concentrations: T1 50 nM, T2 60 nM, T3 150 nM (red curve on the right plot). T1 50 nM, T2 120 nM, T3 150 nM (blue curve on the right plot). Bst pol 4 u/ ml, Nt.BstNBI 25 u/ml.

As it is shown the lag-period of the growth was decreased from 80 min to 30 min when digestion time was increased from 10 min to 90 min. The slope of the curves corresponded to different times of the RecJf treatment was not changed and found similar to normal growth. In the following experiments templates T2 and T3 were processed in the same pot, producing α and β to recruit inhibitor (Inh) with linear growth of β and Inh, leading to the inhibition of the first action, exponential growth. Further digestion step contributes to next exponential amplification (Figure 38, right plot).

Concentrations of templates are very important for production of stable oscillations [Montagne] since producing amount of inhibitor directly affects the rate of inhibition and thus the rate of digestion. 3-fold excess of T3 contributes to long time scale of the experiment (Figure 38, right). Moreover, concentration of T2 affects growth of β, so comparing red and blue curves concerned with 60 and 120 nM of T2, respectively, one could conclude that increasing T2 concentration prevents inhibition action.

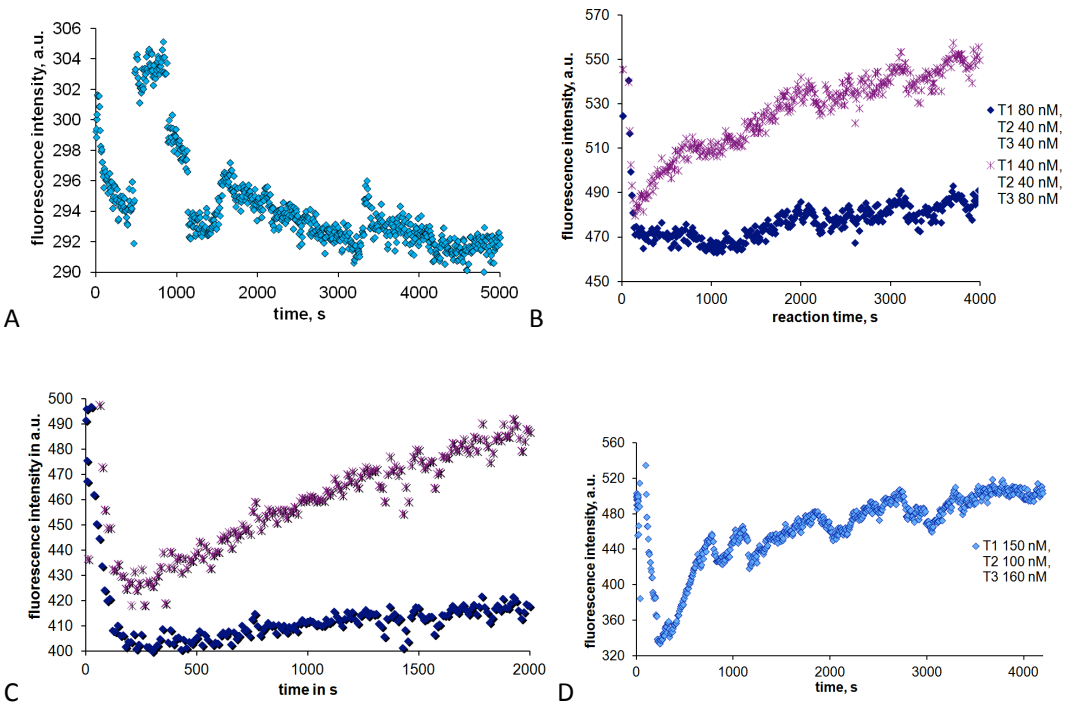

Figure 22: Oscillations. All the reactions shown were performed at 40°C, initiated with 1 nM αT1 and monitored using EvaGreen induced fluorescence as it is stated before. A. Optimal concentrations found: Bst 4 u/ml, Nt.BstNBI 25 u/ml, RecJf 30 u/ml, T1 40 nM, T2 40 nM, T3 40 nM. B. Oscillations were disturbed by increasing of Bst, Nt.BstNBI and RecJf concentrations up to 20, 100 and 75 u/ml. C. No oscillations observed in the system similar to one illustrated as B; T2 200 nM. D. Disturbed oscillations at Bst, Nt.BstNBI, and RecJf concentrations 8 u/ml, 40 u/ml, 30 u/ml, respectively.

When T1, T2, and T3 were in equal concentrations, 40 nM, we observed at least two resolved oscillations, with period 30 and 25 min, and sharp growth in the beginning (Figure 39A). Increasing of T2 concentration up to 200 nM at constant concentrations of T1 and T3, respectively, gives normal product growth (Figure 39C). That is the similar case to one illustrated at Figure 38 when lower T2 concentration contributed to the inhibition. Inhibition action follows peak of β concentrations, so at high T2 concentration formation of non productive βT2 complexes prevents effective inhibitor growth. Enzyme concentrations varied also show influence on the oscillation behaviour, as higher enzymes concentration as more disturbed the oscillation (B, D). This is found in a good agreement with Montagne results.

1.11 Integration of triplex-based DNA ligation & amplification into microfluidic environments

Triplex state was detected by CGE in Pluronic thermoresponsive hydrogel matrix and was well resolved from single and double strands within 10-15 min. Almost complete triplex formation at pH 5.0 and no triplex formation upon pH jump to 7.5, results being in an agreement with pH-dependence in the CD spectra (Figure 40).

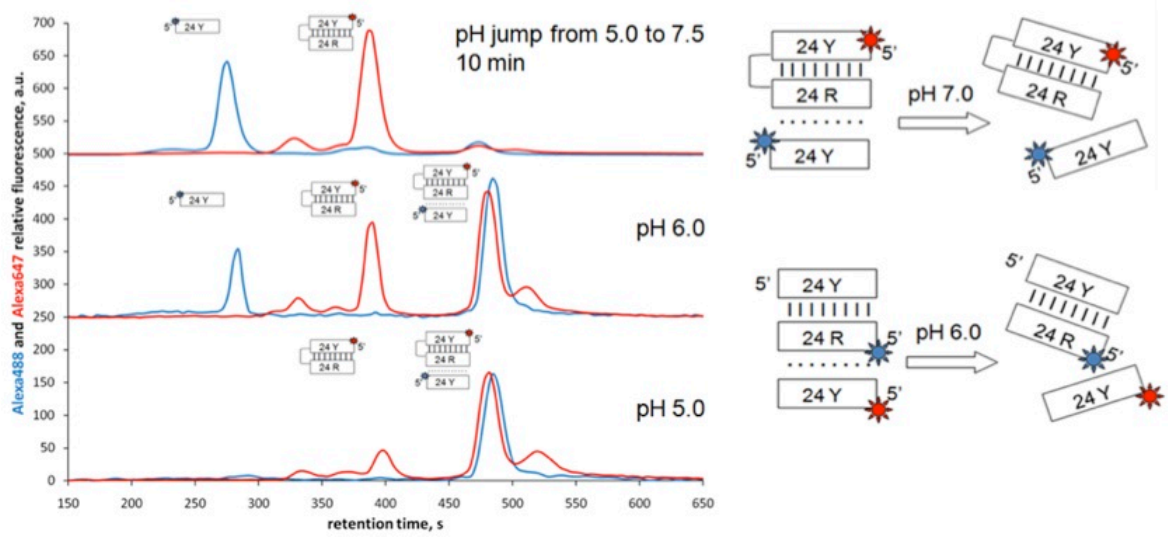

Figure 23: CGE plots at particular pH and isothermal transitions assigned in accordance to initial pH-dependent CD conformation assay (see WP1).

Triplex band was overlapped with the band of by-product probably involving formation of hybrid homopurine homopyrimidine DNA intermolecular complex. This complex displayed similar pH-dependence of CD spectra thus involving cytosine protonation for its formation. Fraction of by-product was calculated at different DNA concentrations and conditions would be optimized for further applications. The triplex yield was 45, 55 and 70 % for systems containing 0.5, 1 and 2 equivalents of DNA sequence **14**, respectively.

Kinetics of triplex formation.

Further work involves fluorescence quenching assay for on-line monitoring of triplex formation (see also WP1). At low pH Hoogsteen strand forms triplex with hairpin DNA as well as brings the attached black hole quencher (BHQ-3) in the vicinity of Alexa647 dye. Kinetics of triplex formation was assigned by fluorescence quenching and from plots obtained for different DNA concentration the reaction order is calculated.

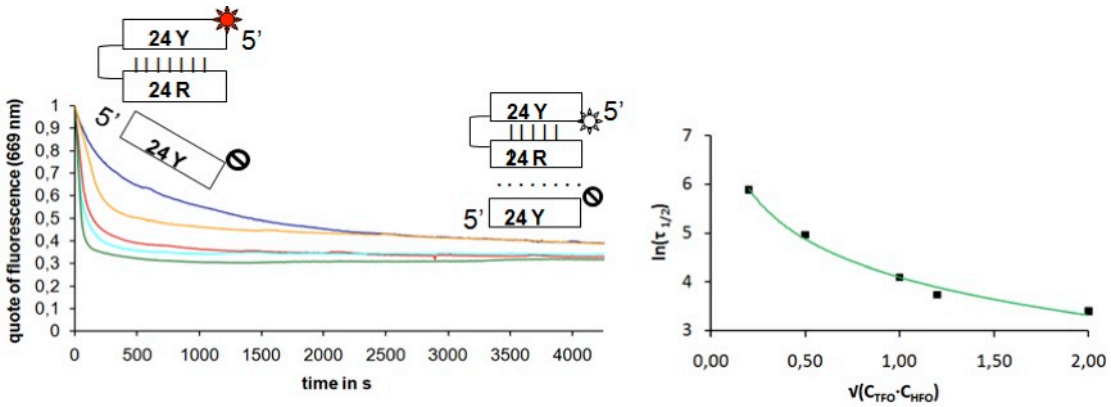

Figure 24: Time-trace plots at pH 6.0 for concentration of hairpin DNA template and TFO varied from 0.2 to 2.0 μM keeping equimolar ratio between strands. Analysis of reaction half-time dynamics for different oligonucleotide concentration is shown at the right side.

The 1st order reaction was found at pH 6.0. Triplex was formed very fast (half-time 42 sec for 1 μM triplex concentration (Figure 41)). Although lower pH contributes to triplex stability, the kinetics revealed for pH 5.0 show higher half-times for the same triplex concentration as compared to pH 6.0, particularly 4.5 min (60-fold) for 1 μM triplex concentration.

pH-cycles: real-time monitoring in cuvette and in the Chemical microprocessor (in prep.)

We would be able to look inside the one-pot reaction at particular stage based on quenching

effect built in leaving group for disulphide ligation monitoring (RUBb) and involving EvaGreen fluorescence for product growth monitoring. Using our dye-quencher analysis of triplex formation and dissociation we made series of fluorescence quenching and enhancement, respectively, by cycling pH. Low and high pH was achieved in cuvette by adding hydrochloric acid and sodium hydroxide, respectively, or produced electrochemically on chip. Unfortunately in first case we created salt gradient and pH was cycled roughly between 5.6 and 7.5 although the quenching was very pH-dependent (Figure 42).

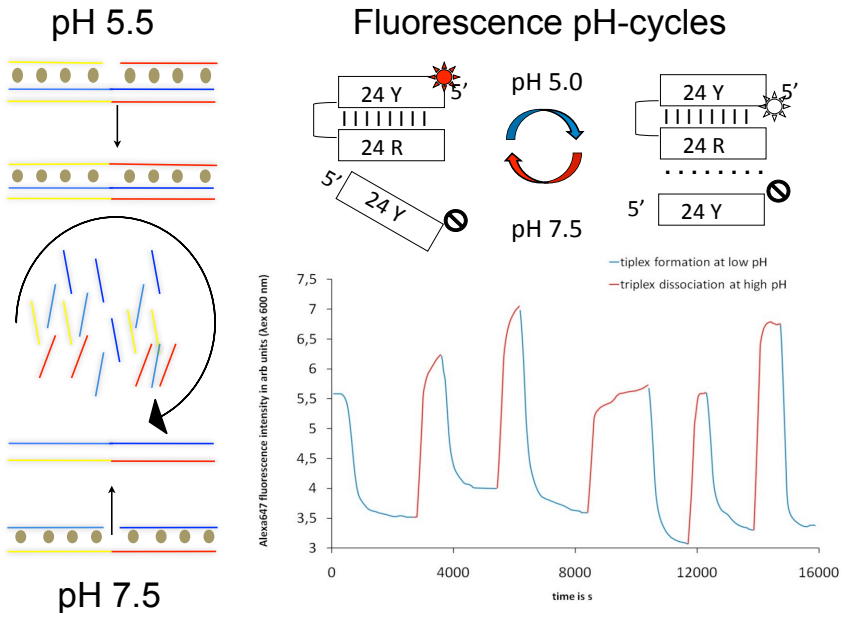

Figure 25: pH-cycles. A. Contribution of pH-cycles to template-directed ligation and replication. B. Examination of triplex formation and dissociation by fluorescence cycling pH between 5.0 and 7.5. 5'Alexa647 fluorescence is quenched when triplex is formed and enhanced when third strand carrying 3'BHQ is released.

pH-switch produced electrochemically (see also WP3 and the following chapter) would contribute to two side ligation, within duplex and triplex at high and low pH, respectively. Working with pH-switchable dyes (e.g. Carboxy-SNARF) would contribute to exact pH control because pH has great value on kinetics and yield of triplex formed.

1.12 Electrochemically stimulated pH changes in a homogeneous solution using microelectrodes

As reported by Kohlheyer et.al.[4] the generation of oxygen and hydrogen bubbles in microfluidic free-flow electrophoresis chips has been suppressed by adding a redox-couple to the electrolyte flowing along the electrodes. Quinhydrone (QH), which is a complex between hydroquinone (H_2Q) acting as an electron donor and p-benzoquinone (BQ) acting as an electron acceptor. QH is known for its application in pH sensor and related devices and the QH electrode reactions are given by[5]

anodic reaction: $C_6H_4O_2H_2 \rightarrow C_6H_4O_2 + 2H^+(aq) + 2e^-$ and

cathodic reaction $C_6H_4O_2 + 2H_2O + 2e^- \rightarrow C_6H_4O_2H_2 + 2OH^-$

[4] Kohlheyer, D., Eijkel, J. C. T., Schlautmann, S., Van Den Berg, A., & Schasfoort, R. B. M. (2008). "Bubble-Free Operation of a Microfluidic Free-Flow Electrophoresis Chip with Integrated Pt Electrodes. Analytical Chemistry, 80(11), 4111–4118.

[5] van der Schoot, B.; Bergveld, P. Sens. Actuators 1985, 8, 11–22.

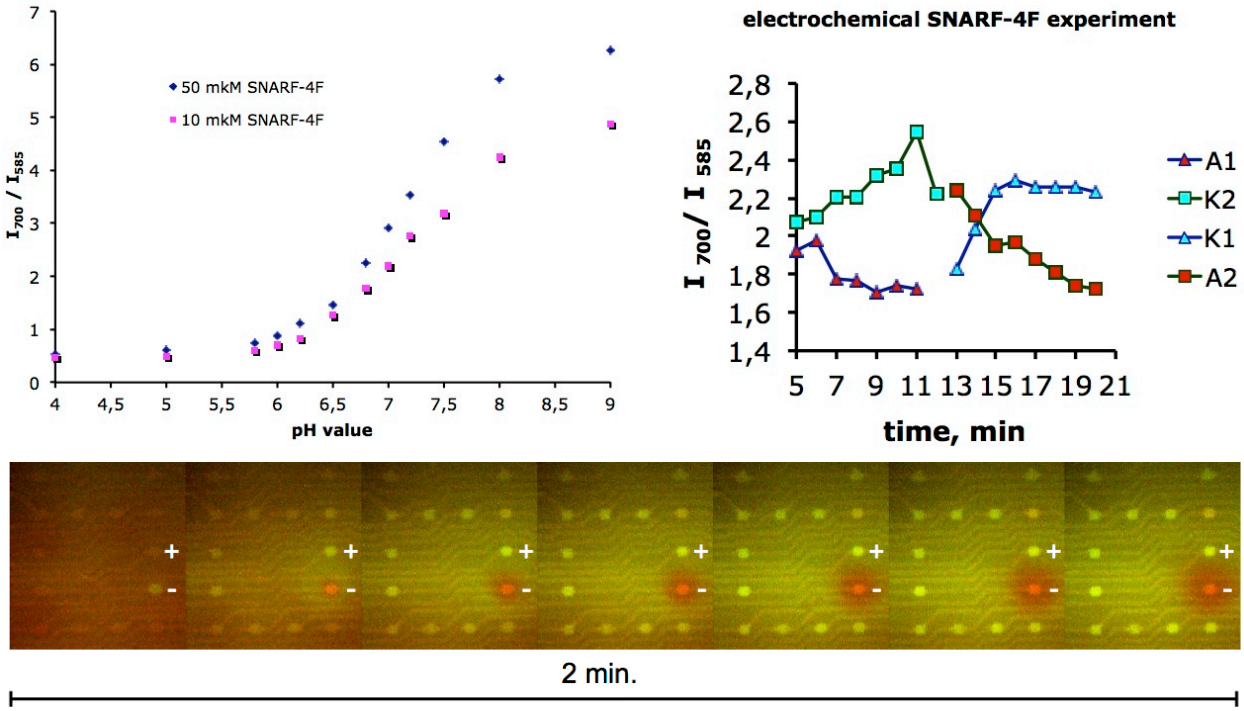

Figure 26: Quinhydrone redox-couple detected by pH-dependent SNARF fluorescence. Left: A calibration curve was obtained in a 1536 well microtiterplate format (4-fold magnification) in 25 mM Sörensen buffer for pH 4.0-9.0. Although, SNARF-4F has a pKa 6.4, the inversion point on both plots for different concentration of SNARF-4F is concerned with pH 7.5). Right: electrochemical pH changes on microelectrodes detected by SNARF fluorescence. Red coloured data points are for anode and blue/cyan - for cathode mode.
Fluorescence image series: red and green colours indicate 700 nm and 585 nm emission filters, respectively. Two electrodes on the right hand side of the electrode array were on. Accordingly to high pH produced at negative electrode, we observed the SNARF wavelength shift towards 700 nm.

Figure 43 demonstrate first tests of electrochemical pH changes using a 25 mM Sörensen buffer at pH 7.0. The first 5 minutes were associated with dye concentration and repulsion at positive and negative electrodes, respectively, which indicates that dye was negatively charged at pH 7.0.

After that fluorescence images were acquired using two emission filters (585 nm and 700 nm), between 5-12 min electrodes were switched at one mode and then they were inverted. Thus you have one and half pH-cycles (7.0 - 7.2 - 6.7, and 7.0 - 6.7 - 7.2). The pH jump is found reproducible in time and on both electrodes. Half a unit is comparatively high, taking into account that it takes place in buffered solution (25 mM, Sörensen buffer, pH 7.0).

BQ and HQ without any additives hold pH 4.5 – 5.0, thus pH changes produced at the positive electrode (figure 42 bottom) do not affect significantly fluorescence of SNARF-4F (figure 42 left plot, fluorescence is not changed in the pH range 4.0 – 5.5). This can explain why the approach is more sensitive to pH changes towards higher values contributing to "asymmetric" behaviour of two electrodes (bottom). We observed an overall pH change in the pure Quinhydrone redox-couple solution 1.5 units (pH 4.5-6.0).

As it is described in figure 41, for pH cycles we use Alexa647/BHQ-3 FRET fluorophor combination, which leads to fluorescence quenching only in triplex. In separate control experiments we showed that it never occurs at pH > 7.0 even after concentration (not shown).

In the following experiment we have done pH cycles on triplex formation/dissociation involving pH changes induced electrochemically via BQ reduction and HQ oxidation. The corresponding pH changes occur in the bulk in array of 12 microelectrodes creating a profile of fluorescence (figure 44). On the contrary, the electrode surface display only repulsion (negative) or attraction (very short time, positive) of DNA. Moreover, the overall process rate

is limited by appropriate changes of pH, and

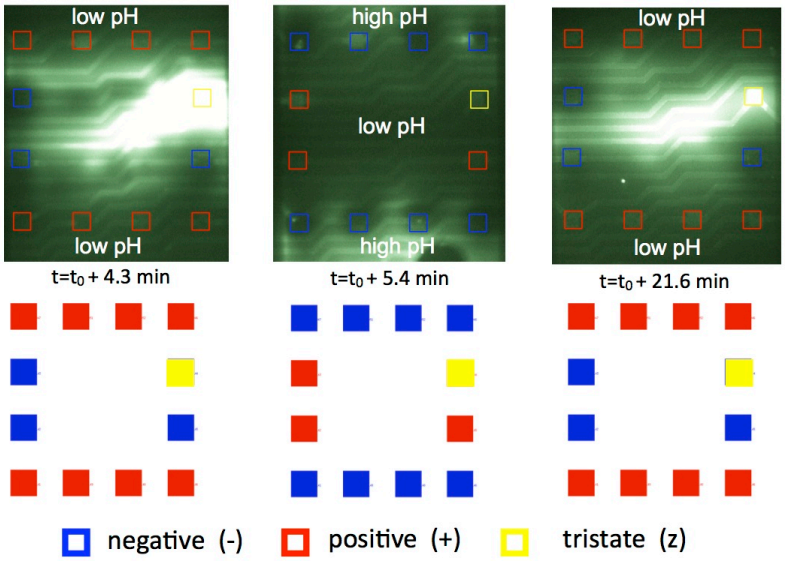

Figure 27: The formation of triplex involving fluorescence quenching is shown at positive electrodes, and the triplex dissociation involving fluorescence enhancement – at negative electrodes. Protons required for cytosine protonation in triplex third strand were produced by HQ oxidation and uptaken via BQ reduction contributing to corresponding pH changes at positive and negative electrodes, respectively. Electrode configuration is shown below fluorescence image, the process was real-time monitored, inverting electrodes at the specified time. Electrochemical conditions: 1.7 V, 100% normal duty, 20% active duty.

1.13 New application using the core functions Electronically Programmable Chemical Matrix - Full DNA Processor

Figure 45 shows the final mask design for the microfluidic integration to do a complete cycle of droplet reaction, extraction to gel, product separation in gel as well as the content transport between two micro reaction chambers.

External regulation and synchronization is achieved through the electronic control of transport of informational molecules between the two locations. This is the requirement for electronically regulated isothermal amplification reactions in a microfluidic environment.

The full DNA Processor couples up to 8 separate ECCells for DNA processing reactions via DNA exchange and should allow separate regulated reactions and programmable selective DNA transfer via flexible gel separation tracks between reactors.

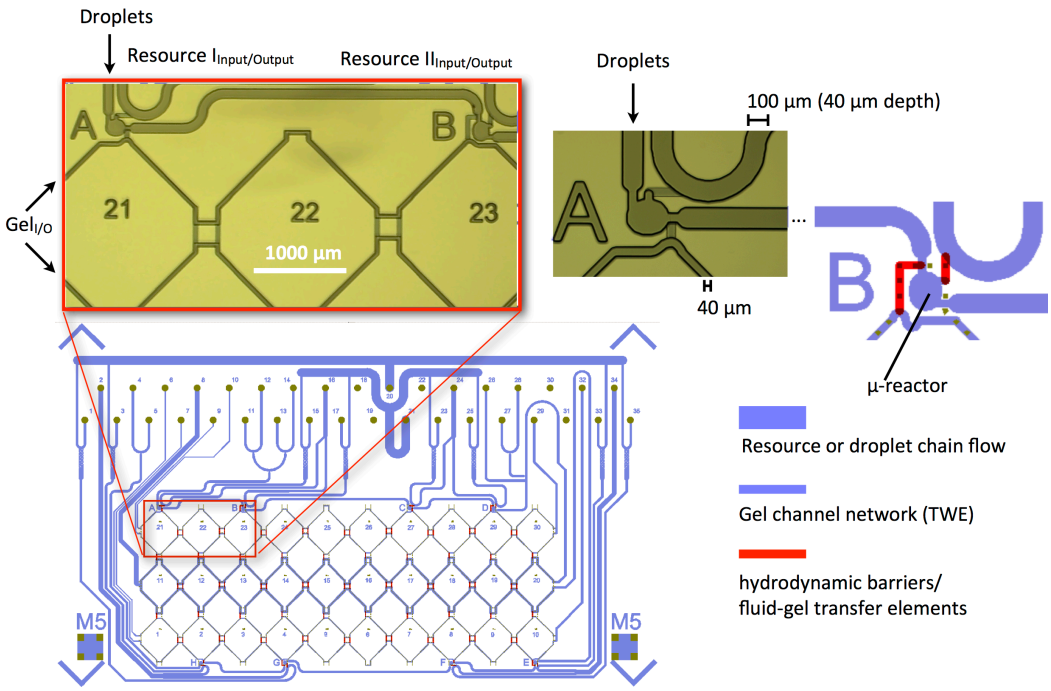

Figure 28: Final mask design for the microfluidic integration to do a complete cycle of droplet reaction, extraction to gel, product separation in gel as well as the content transport between the two chambers. The light microscopic images show the master structures for micromoulding process in PDMS.

1.14 Prototype frameworks in micro fluidics (SDU)

In order to interface an evolving a self-contained chemical system with an evolving computer microprocessor system (for chemical ICT), we are developing prototype frameworks in microfluidics to serve the several necessary functions of the chemical system: 1) droplet generation with varying controlled inputs, 2) droplet detection based on colorimetric, size, or fluorescent signal, 3) droplet manipulation and selection based on internal microfluidic architecture or electronics, and 4) droplet recycling where created, detected and selected droplets are recycle through the microfluidics layer for iterative droplet evolution cycles based on controlled fusion and fission events, see figures. The chemical system (chemical wetware) and computer system (MEMES hardware) are designed to work together to make a chemical ICT evolving system, as described in detail in **WP4**.

A lot of initial effort in the project was put into establishing a stable and flexible microfluidic system. Since no prior experience was available at NanoSYD, development had to start more or less from scratch. This included a widespread literature study and experimentation with different production methods. After considerable time and effort we settled on a system utilizing simple flexible polymer chips made of PDMS. These chips are made via molding and replication of an inverted epoxy-based master structure formed in SU8. The epoxy thickness defines the height of the microfluidic channels. The SU8 is a photosensitive epoxy and by exposing it to UV light through a photolithographic mask it can be developed to produce a certain structure (see fig. 46A for an example of a structure). A novel approach[6] is developed where simple black and white photonegatives are used as photo-masks (see fig. 46B). While this approach has some limitations regarding resolution (minimum structure size ~40 µm), this is outweighed by the low cost and great flexibility deriving from the fact that up to 36 different designs can be made in one go. Another advantage of using the soft PDMS polymer is the easy connectivity of the chips since its forms a tight seal around external

[6] Simple photolithographic rapid prototyping of microfluidic chips, J.D. Hoyland and C. Kunstmann-Olsen, *Microelectronic Engineering (2012), in review*

connectors.

In order to gain a better understanding of how to control the flow of liquids in the laminar flow regime that dominates microfluidic systems, investigations into hydrodynamic focusing were undertaken.[7] This covers both experimental and theoretical work, but also finite element modeling in COMSOL (see fig. 46C). COMSOL has also been used to study how flow parameters influence droplet formation, even though the models are still quite simple (see fig. 46D).

In order to realize a life-cycle environment for droplet based protocells several individual microfluidic components and functions need to be considered. The PDMS chip system with matching interconnects (using stainless steel tubes and 200 µm I.D. FEP tubes, see fig. 46E and 46F.) are designed to be modular and each life step can hence be treated individually. The following functions have been investigated:

- Oil droplet generation with appropriate surfactant molecules for stabilization (see fig 46G) – using hydrodynamic focusing to pinch of droplets
- Stabilization of Nitrobenzene droplets allow for easy harvesting of droplets (see fig. 46H) for later used while size distributions are maintained (see fig. 46)
- Chips for generating up to 3 different droplet species designed (see fig. 46J)
- Chips for separating droplet populations for individual operation – using both air bubbles (fig. 46K) and ionic liquids (fig. 46L)
- Ongoing work on selected chemical fusion of droplets by change of local pH (using HCl or NaCl), see fig. 46M
- Development of flow cytometric microfluidic chips for detection of fluorescence as function of successful fusion (see fig. 64N, 46O)
- Initial design of a multifunctional chip for "droplet evolution" to support droplet formation, fission, fusion, reactions, detection and selection (see Fig. 46P).

[7] Influence of geometry on hydrodynamic focusing and long-range behavior in PDMS microfluidic chips, C. Kunstmann-Olsen, J.D. Hoyland and H.G. Rubahn, *Microfluidics and Nanofluidics (2011), DOI: 10.1007/s10404-011-0923-1*

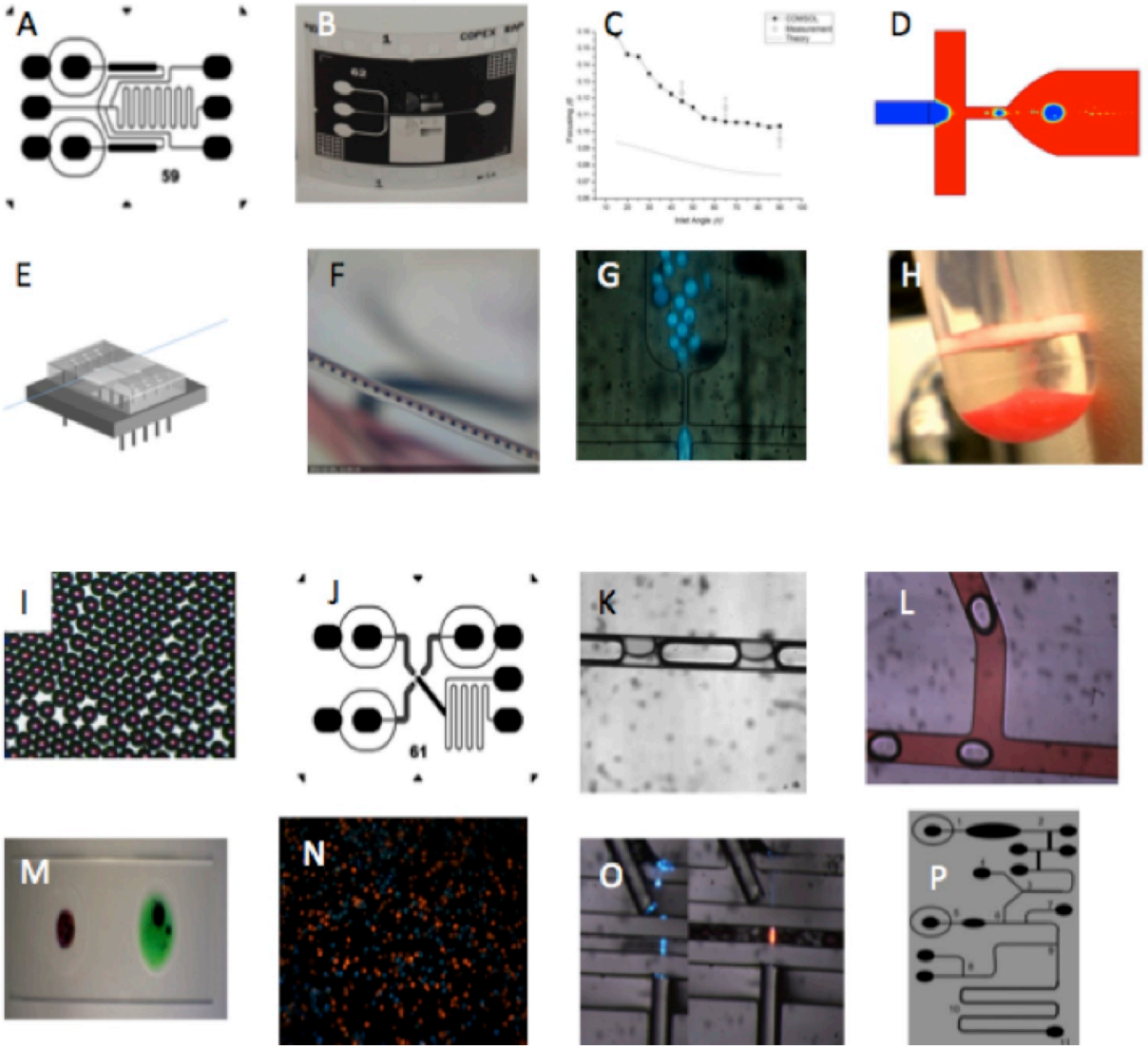

Figure 29: Prototype frameworks in micro fluidics.